Supplement of

Mercury in the Free Troposphere and Bidirectional Atmosphere-Vegetation Exchanges – Insights from Maïdo Mountain Observatory in the Southern Hemisphere Tropics

Alkuin M. Koenig et al.

Correspondence to: Alkuin Koenig (alkuin-maximilian.koenig@univ-grenoble-alpes.fr)

Sect. S1 : Regional and synoptic transport to Maïdo

10 We characterized regional and synoptic scale transport to Maïdo during our measurement period with FLEXPART-AROME, even though no FLEXPART-AROME output (from Verreyken et al., 2021) is available before November 2017. Transport to Maïdo was dominated by easterlies in all seasons (Figure S1), reflecting that Réunion is generally under a trade wind regime (Foucart et al., 2018). However, there were certain second-order seasonal differences: During November 2017, air mass origin was comparatively more mixed, with important

15 westerly and north-westerly contributions. In DJFM (Dec. 2017 – Mar. 2018), there were next to no southerly, but some northerly contributions, while the opposite was the case for AMJ (Apr. 2017 – Jun. 2018), with next to no northerly but important southerly contributions.
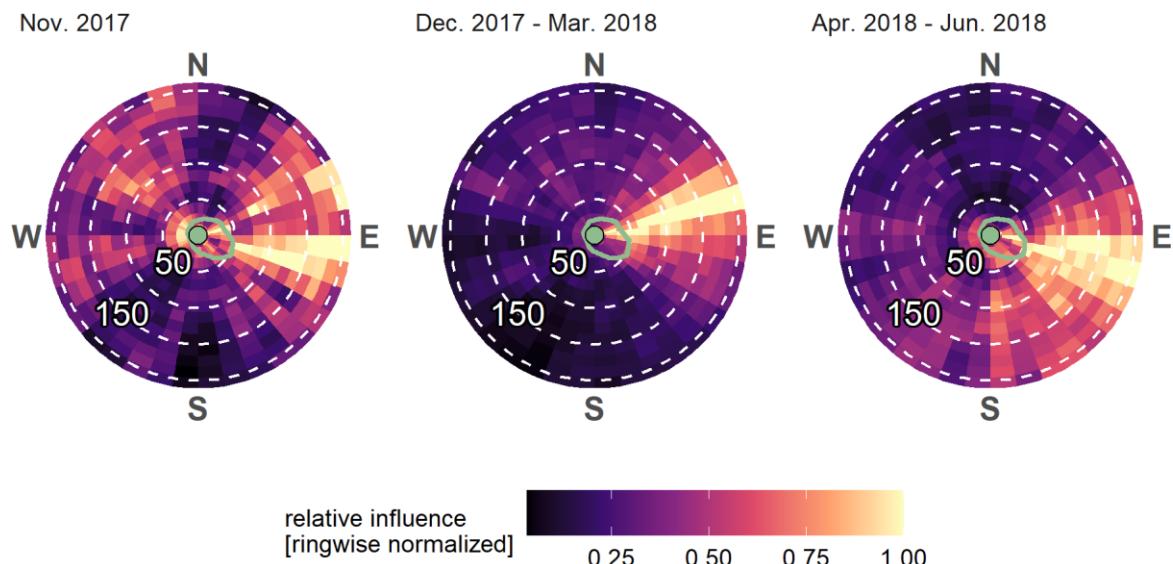
Figure S1. Transport to Maïdo as estimated with FLEXPART-AROME for the period of overlap between Hg

20 **observations and FLEXPART-AROME output. The green outline shows Réunion Island, the green point Maïdo observatory. Concentric circles give the distance to Maïdo observatory in km (see numbers). The colour scale is normalized so that "1" corresponds to the most influential cell within the respective ring (the normalization was done for each ring individually). Regional and synoptic transport to Maïdo is mostly dominated by easterlies, corresponding to trade winds.**

25

Sect. S2 : Diurnal variation of GEM and specific humidity during cyclonic storms

Maïdo was affected by several cyclonic storms during our measurement period, the most noteworthy being: Ava (~13 days, 27.12.2017 – 09.01.2018), Berguitta (~11 days, 09.01.2018 – 20.01.2018), Dumazile (~6 days, 01.03.2018 - 06.03.2018), Eliakim (~7 days, 13.03.2018 – 20.03.2018) and Fakir (~5 days, 20.04.2018 –
30   25.04.2018) (http://www.meteo.fr/temps/domtom/La_Reunion/webcmrs9.0/anglais/index.html, last access: 10/08/2022).

To investigate the impact of cyclonic storms on GEM dynamics at Maïdo, we compared, for three storms for which continuous GEM data were available (Ava, Dumazile, Eliakim), the diurnal variation of GEM and specific humidity during the storm with the respective diurnal variation 5 days before and after the storm (Figure
35   S2). We found that diurnal variation of GEM and specific humidity were largely suppressed during each of these three cyclonic storms. In all cases, both GEM and specific humidity remained particularly high during the nighttime. This suggests that, during cyclonic storms, nighttime data is not representative of the lower free troposphere (LFT), and that GEM in the LFT is lower than in the marine boundary layer.
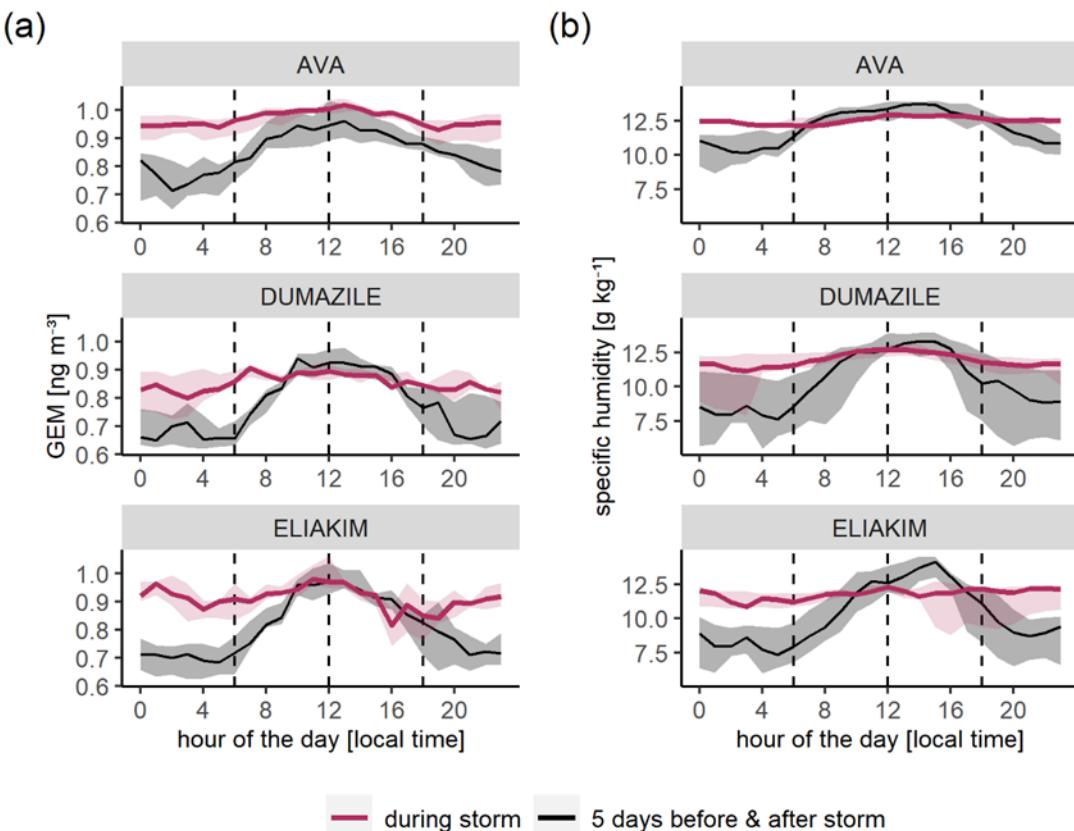
40   **Figure S2. Median diurnal cycles of (a) GEM and (b) specific humidity during the cyclonic storms Ava, Dumazile, and Eliakim. The median diurnal cycle 5 days before and after each storm is shown in black. The shaded area encloses the 25th to 75th percentiles. Diurnal cycles of GEM and specific humidity were notably suppressed during cyclonic storms.**

Sect. S3 : Data table for gaseous elemental mercury (GEM) at Maïdo

45   Monthly averaged GEM at Maïdo for different data selections is given in Table S1 below. Nighttime data corresponds to all data taken between 23:00 and 5:59 local time. LFT selection corresponds to nighttime data in dry air masses (specific humidity < ERA5 median monthly specific humidity at Maïdo coordinates and 800 hPa).

Table S1. GEM at Maïdo for different data selections (all data, nighttime, LFT). Monthly averages correspond to all
50   **data taken between the first and last day of the respective month.**

month	data selection	mean [ng m^{-3} STP]	standard deviation [ng m^{-3} STP]	# hourly averages	standard error [ng m^{-3} STP]
2017-09	all data	0.859	0.12	633	0.005
2017-10	all data	0.922	0.12	665	0.004
2017-11	all data	0.933	0.11	694	0.004
2017-12	all data	0.786	0.1	738	0.004
2018-01	all data	0.879	0.11	391	0.006
2018-02	all data	0.781	0.096	581	0.004
2018-03	all data	0.827	0.12	708	0.004
2018-04	all data	0.798	0.079	624	0.003
2018-05	all data	0.869	0.072	531	0.003
2017-09	nighttime	0.793	0.099	193	0.007
2017-10	nighttime	0.837	0.09	197	0.006
2017-11	nighttime	0.872	0.12	210	0.008
2017-12	nighttime	0.687	0.076	217	0.005
2018-01	nighttime	0.824	0.11	112	0.01
2018-02	nighttime	0.707	0.086	172	0.007
2018-03	nighttime	0.761	0.12	213	0.008
2018-04	nighttime	0.758	0.062	181	0.005
2018-05	nighttime	0.827	0.054	157	0.004
2017-09	LFT	0.74	0.076	103	0.007
2017-10	LFT	0.818	0.088	137	0.008
2017-11	LFT	0.819	0.083	94	0.009
2017-12	LFT	0.651	0.054	122	0.005
2018-01	LFT	0.628	0.025	9	0.008
2018-02	LFT	0.649	0.1	54	0.01
2018-03	LFT	0.679	0.064	121	0.006
2018-04	LFT	0.732	0.053	92	0.006
2018-05	LFT	0.79	0.043	71	0.005

Sect. S4 : Estimation of air mass mixing with FLEXPART-AROME

To estimate the fraction of sampled air masses corresponding to the LFT and the BL, respectively, we used the clustered output (trajectories.txt; Pisso et al., 2019) from FLEXPART-AROME (see methods) combined with ERA5 reanalysis data (Hersbach et al., 2020).

We first estimated, on an hourly basis, the fraction of air masses corresponding to the LFT and the boundary layer (BL) by the following criteria:

- The fraction of all FLEXPART particles outside the boundary layer (information contained in trajectories.txt) was assigned to the LFT (i.e. $Particles_{outside\ BL} = fraction_{outside\ BL} * Particles_{all}$)
- The remaining particles were assigned to the BL

BL particles were then additionally split into particles belonging to either the marine boundary layer (MBL) or the (mountain) planetary boundary layer (PBL) following the criteria below (compare to Figure S3):

- All BL particles over geographical cells with an underlying orography below the mean ERA5 boundary layer height of the surrounding ocean were assigned to the MBL. This means, effectively, that we assumed that the island is submerged into the MBL up to the mean boundary layer height of the surrounding ocean (as obtained from ERA5).
- All other BL particles were assigned to the mountain PBL.

Only when estimates on water-soluble reactive mercury (RM) were concerned, particles belonging to the LFT were additionally split into either particles coming from clouds or particles coming from the cloud-free LFT, as described below:

- LFT particles were assigned to clouds proportionally to the cloud coverage in the respective cell, as obtained from ERA5 (i.e. $Particles_{clouds} = Particles_{LFT} * fraction_{clouds}$). Low, middle, and high clouds were treated separately, for which the altitude of the FLEXPART particle cluster centroid was considered.
- All remaining LFT particles were assigned to the cloud-free LFT
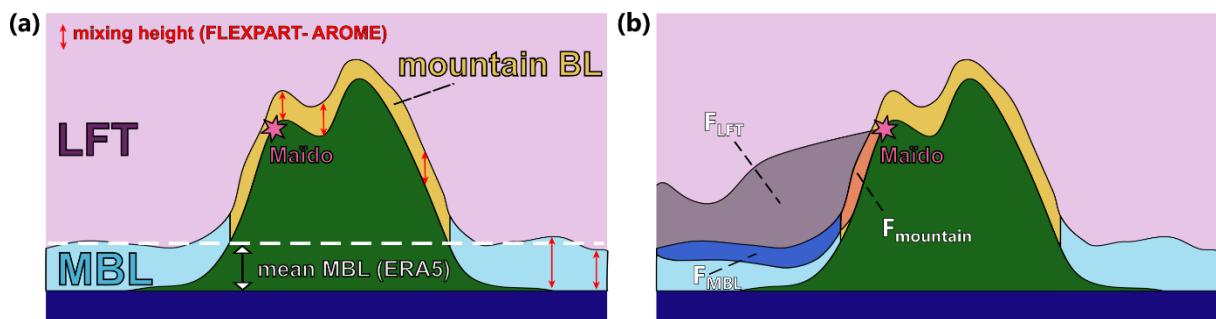
Figure S3. Scheme describing the estimation of mixing between LFT, MBL, and (mountain) BL. (a) Definition of the MBL, the LFT, and the (mountain) BL. We assumed that the island is submerged into the MBL up to the mean MBL of the surrounding ocean (dashed white line, as obtained from ERA5). (b) An example on the estimation of the fraction of air masses coming from the LFT (F_{LFT}), the MBL (F_{MBL}), and the (mountain) BL ($F_{mountain}$) for a hypothetical dispersion run result.

85   Finally, for each FLEXPART-AROME dispersion run, we only considered the last 8 hours before arrival at Maïdo to estimate air mass mixing. In addition, we applied a weighting function of inverse proportionality to the time until arrival. This means, for example, that the position of FLEXPART particles 1 hour before arrival is twice (four times) as influential on the estimated air mass mixing between MBL and LFT as the position of FLEXPART particles 2 hours (4 hours) before arrival. We find that the resulting modeled fraction of air coming

90   from the MBL agrees well with the observed diurnal variability of DMS (Figure S4).

While our general results on the role of mixing processes and the potential importance of photo-reemission are not sensitive to choices for cutoff time and weighting, the most likely surface reemission flux obtained from inverse modeling is. To address uncertainties associated with these choices, three different values for the cutoff time (6 hours, 8 hours, and 10 hours), and three different weighting functions (no weighting, inverse

95   proportionality to time until arrival, inverse proportionality to the square of time until arrival) have been considered to estimate the confidence interval for the Hg reemission flux in a Monte Carlo approach (Sect. S6).
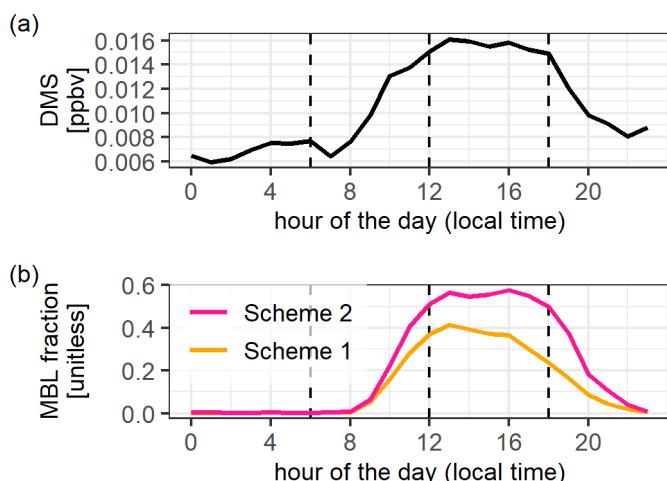
Figure S4. Comparison between observed DMS diurnal cycle and modeled diurnal cycle of MBL influences.
(a) Observed mean DMS diurnal cycle for days characterized by a marked GEM diurnal variation (Group 1 days, see

100   **section 3.3.1 of the main text).**
(b) Modelled mean diurnal cycle of the fraction of air masses coming from the MBL, for the same days as in (a)
(Group 1 days). Scheme 1 corresponds directly to F_{MBL} in Figure S3b. For Scheme 2 it was assumed that mixing
proportions between MBL and LFT are identical for the entirety of the mountain BL, and that, without surface
influences, mountain BL air itself is ultimately a mix of LFT and MBL air, yielding:

105   **$F_{MBL}(Scheme\ 2) = F_{MBL}(Scheme\ 1)/(1 - F_{mountain})$ (Scheme 2 was used for modeling of GEM diurnal cycles, see Sect. S5).**

Sect. S5 : Models of GEM diurnal variation

Sect. S5.1 : Two box miding model between LFT and MBL

110 To estimate the expected GEM diurnal variation if only mixing processes are considered we started with
Equation S1 below.

$$GEM_{maido} = F_{MBL} \cdot GEM_{MBL} + F_{LFT} \cdot GEM_{LFT} + F_{mountain\ BL} \cdot GEM_{mountain\ BL} \qquad \textbf{Equation S1}$$

Where F_{MBL}, F_{LFT}, and $F_{mountain\ BL}$ are the fraction of air masses coming from the MBL, the LFT, and the
mountain BL, respectively (see Sect. S4). GEM_{maido}, GEM_{MBL}, GEM_{LFT}, and $GEM_{mountain\ BL}$ are GEM

115 concentrations at Maïdo (observed), in the MBL surrounding Réunion Island, in the LFT, and in the mountain
BL, respectively.

We then assumed that, if only mixing between LFT and MBL is considered, GEM concentrations observed at
Maïdo are representative of GEM concentrations in the entire mountain BL (i.e. $GEM_{maido} = GEM_{mountain\ BL}$).
This means, effectively, that we assumed that the mixing status (between LFT and MBL air) is, on average, the

120 same for the entire mountain BL. This assumption yields Equation S2 (note that $F_{MBL} + F_{LFT} + F_{mountain\ BL} = 1$).

$$GEM_{maido} = GEM_{mountain} = \frac{F_{MBl}}{F_{MBL}+F_{LFT}} GEM_{MBL} + \frac{F_{LFT}}{F_{MBL}+F_{LFT}} GEM_{FT} \qquad \textbf{Equation S2}$$

Finally, for our results in section 3.3.2, Equation S2 was integrated over the last 8 hours before trajectory arrival,
i.e.:

125 $$GEM_{maido}(t) = \sum_{k=0h}^{8h} \left(\frac{F_{MBl}(t-k)}{F_{MBL}(t-k)+F_{LFT}(t-k)} GEM_{MBL}(t) + \frac{F_{LFT}(t-k)}{F_{MBL}(t-k)+F_{LFT}(t-k)} GEM_{FT}(t) \right) \qquad \textbf{Equation S3}$$

Sect. S5.2 : Adding photo-reemission to the mixing model

To estimate the expected GEM diurnal variation if parametrized photo-reemission from the island is considered
in addition to mixing processes, we added a photo-reemission term to the mixing model described with Equation

130 S2 (see above), obtaining Equation S4.

$$GEM_{maido} = \frac{F_{MBl}}{F_{MBL}+F_{LFT}} GEM_{MBL} + \frac{F_{LFT}}{F_{MBL}+F_{LFT}} GEM_{FT} + c * SRR * RAD \qquad \textbf{Equation S4}$$

Where RAD is solar radiation as measured at Maïdo (in W m^{-2}) and c is an unknown scaling constant (in ng J^{-1})
describing the relationship between solar radiation and Hg reemission, whose most likely value (under the
hypothesis of surface reemission) was determined in an inverse modeling approach (see section 3.3.3 of the main

135 text). SRR is the FLEXPART-AROME-derived source-receptor relationship between the islands surface and
Maïdo observatory (see methods), given in units of s m^{-1} so that the term $c * SRR * RAD$ has units of
concentration (ng m^{-3}).

SRRs were calculated, analogously to Verreyken et al. (2021), by dividing the FLEXPART-AROME-derived
particle residence time by a constant minimal boundary layer height (Seibert and Frank, 2004). In contrast to

140 Verreyken et al., 2021, which did not use the SRR to estimate emission fluxes and used a minimal boundary
layer height of 500 magl, here we used a minimal boundary layer height of 250 magl which, after performing a
sensitivity analysis, we found to be more appropriate for the quantitative estimation of fluxes. While the choice

of the minimal boundary layer height does not affect our overall results and conclusions, it affects the most likely surface reemission flux obtained in the inverse modelling. To address uncertainties associated with the choice of the minimal boundary layer height, three different values (100 magl, 250 magl, 400 magl) have been considered to estimate the confidence interval for the Hg reemission flux (Sect. S6).

For our results in section 3.3.3, we integrated the mixing-related part of Equation S4 over the last 8 hours before arrival (i.e. we considered the position of FLEXPART-AROME particles up to 8 hours into the past), while we integrated the reemission-dependent part of Equation S4 over the last 3 hours before arrival (see Equation S5 below). We only considered the last 3 hours before arrival for photo-reemission as the vegetated surfaces responsible for the observed isoprene and CO_2 diurnal cycles appear to lie relatively close to the station (Verreyken et al., 2021; Callewaert et al., 2022), and because solar radiation observations at Maïdo become, with increasing distance to the observatory, less and less representative for the solar radiation on surfaces in question.

$$GEM_{maido}(t) = \sum_{k=0h}^{8h} \left(\frac{F_{MBl}(t-k)}{F_{MBL}(t-k) + F_{LFT}(t-k)} GEM_{MBL}(t) + \frac{F_{LFT}(t-k)}{F_{MBL}(t-k) + F_{LFT}(t-k)} GEM_{FT}(t) \right)$$
$$+ \sum_{k=0h}^{3h} c * SRR(t-k) * RAD(t-k)$$

Equation S5

Sect. S6 : Confidence interval for Hg reemission flux (Monte Carlo)

The inverse-modeled estimate of the most likely mean net daytime surface Hg photo-reemission flux (see section
3.3.3 of the main text) is sensitive to a variety of parameters, among them the assumed GEM concentrations in
the MBL, the parametrization used to estimate air mass mixing between MBL and LFT with FLEXPART-
AROME (see Sect. S4), and the parametrization used to derive source-receptor relationships (SRRs) with
FLEXPART-AROME (see Sect. S5).

To assess uncertainties and to construct a confidence interval, we used a Monte Carlo approach (see Figure S5).
We first recalculated the most likely mean net daytime Hg photo-reemission flux for a wide range of different
parameter values (1053 parameter combinations in total). We then verified that the median of the resulting
distribution of Hg surface fluxes lies close to our most-likely estimate, and used the 2.5th to 97.5th percentiles of
the distribution as our 95% confidence interval, obtaining $8 - 22$ ng m^{-2} h^{-1}
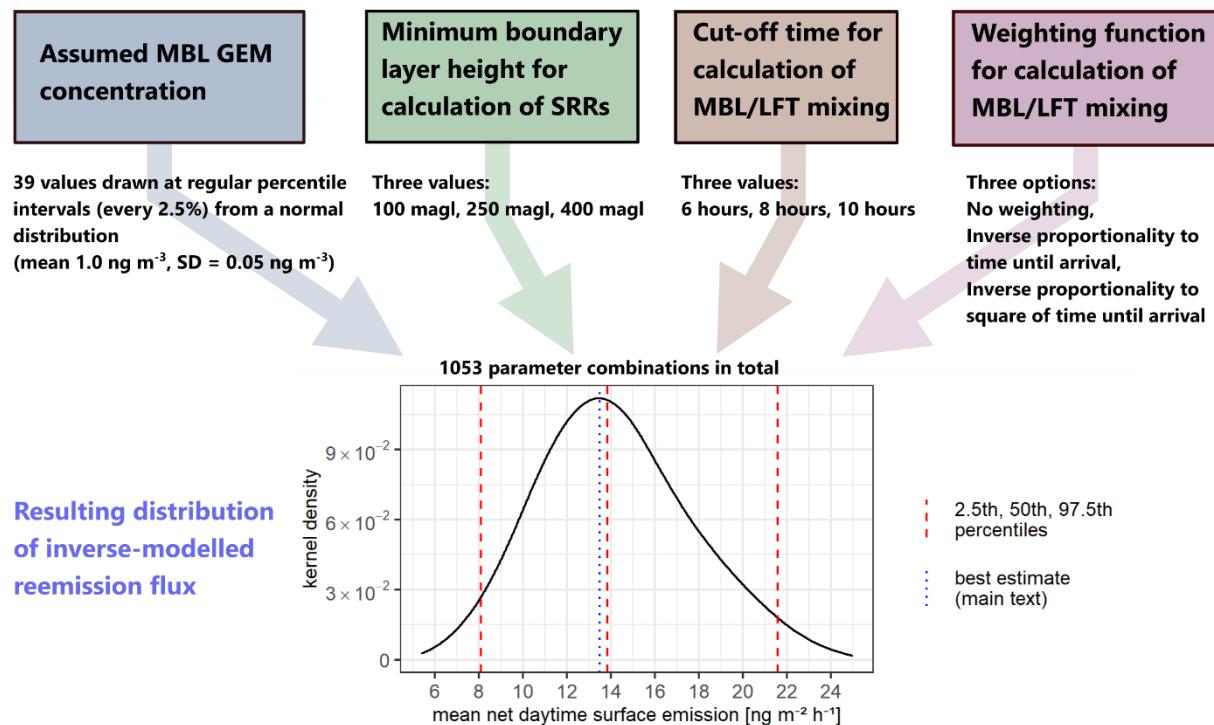
**Figure S5. Monte Carlo approach to estimate uncertainties in the derived Hg photo reemission flux. Inverse modeling
of the most likely (net daytime) photo reemission flux was done for a variety of parameter combinations, constructing
a distribution based on 1053 parameter combinations in total. The three red vertical dashed lines in the inset figure
show the 2.5th, 50th (median), and 97.5th percentiles of the distribution. The blue vertical dotted line shows the most-
likely photo-reemission flux derived in the main text, which lies very close to the median of the distribution.**

Sect. S7 : Data table for reactive mercury (RM) at Maïdo

Maïdo RM data is given in Table S2 below, methodological details are laid out in section 2.2 of the main text.

180 **Table S2. Maïdo RM observations. All times in local time (LT). Concentrations are given at STP.**

Sample ID	Sampling start [LT]	Sampling end [LT]	Sampled STP volume [L]	Sampling time [s]	RM [pg m^{-3}]
S1	2017/09/01 13:35	2017/09/07 09:05	8419	502200	27.0
S2	2017/09/07 14:43	2017/09/13 09:00	8326	497820	12.5
S3	2017/09/13 12:30	2017/09/20 07:05	10084	585300	29.2
S4	2017/09/20 12:40	2017/09/28 09:55	14864	681300	11.2
S5	2017/09/28 12:25	2017/10/11 07:20	15226	1104900	12.0
S6	2017/10/11 16:00	2017/10/19 07:30	14413	660600	16.0
S7	2017/10/19 09:45	2017/10/27 07:45	14923	684000	9.1
S8	2017/10/27 09:30	2017/11/02 07:55	11158	512700	13.4
S9	2017/11/02 10:35	2017/11/10 07:50	14864	681300	14.7
S10	2017/11/10 09:40	2017/11/17 09:25	13178	603900	8.8
S11	2017/11/17 11:30	2017/11/24 07:45	12903	591300	10.6
S12	2017/11/24 09:25	2017/11/30 08:35	9700	515400	14.0
S13	2017/11/30 10:05	2017/12/07 07:20	12982	594900	13.8
S14	2017/12/07 10:05	2017/12/13 05:50	10982	503100	19.8
S15	2017/12/13 07:35	2017/12/21 08:20	15146	693900	4.4
S16	2017/12/21 09:55	2017/12/28 07:55	13047	597600	6.6
S17	2017/12/28 10:25	2018/01/08 10:40	20757	951300	4.2
S18	2018/01/08 12:20	2018/01/22 14:35	7828	1217700	14.3
S19	2018/01/22 17:25	2018/02/05 08:50	16892	1178700	7.6
S20	2018/02/05 09:25	2018/02/13 07:45	14931	685200	4.4
S21	2018/02/13 10:30	2018/02/21 07:10	14715	679200	3.9
S22	2018/02/21 08:30	2018/03/02 08:45	11909	778500	3.4
S23	2018/03/02 10:00	2018/03/08 06:35	11026	506100	4.0
S24	2018/03/08 08:20	2018/03/15 10:35	13377	612900	12.1
S25	2018/03/15 12:15	2018/03/23 08:20	14753	677100	9.8
S26	2018/03/23 10:25	2018/04/03 08:55	20620	945000	7.0
S27	2018/04/03 11:05	2018/04/10 13:10	8278	612300	14.6
S28	2018/04/10 15:15	2018/04/16 21:15	11803	540000	9.9
S29	2018/04/17 17:10	2018/04/25 08:05	14296	658500	4.4
S30	2018/04/25 11:55	2018/05/02 08:40	12943	593100	8.7
S31	2018/05/02 11:20	2018/05/14 08:05	22329	1025100	11.1
S32	2018/05/14 09:40	2018/05/23 14:25	17335	794700	8.0
S33	2018/05/23 16:00	2018/05/31 15:30	14949	689400	9.5
S34	2018/05/31 17:30	2018/06/11 08:20	19022	917400	7.7
S35	2018/06/11 09:50	2018/06/22 08:20	20610	945000	5.2

References

185   Callewaert, S., Brioude, J., Langerock, B., Duflot, V., Fonteyn, D., Müller, J.-F., Metzger, J.-M., Hermans, C., Kumps, N., Ramonet, M., Lopez, M., Mahieu, E., and De Mazière, M.: Analysis of CO2, CH4, and CO surface and column concentrations observed at Réunion Island by assessing WRF-Chem simulations, Atmos. Chem. Phys., 22, 7763–7792, https://doi.org/10.5194/acp-22-7763-2022, 2022.

Foucart, B., Sellegri, K., Tulet, P., Rose, C., Metzger, J.-M., and Picard, D.: High occurrence of new particle formation
190   events at the Maïdo high-altitude observatory (2150 m), Réunion (Indian Ocean), Atmos. Chem. Phys., 18, 9243–9261, https://doi.org/10.5194/acp-18-9243-2018, 2018.

Hersbach, H., Bell, B., Berrisford, P., Hirahara, S., Horányi, A., Muñoz-Sabater, J., Nicolas, J., Peubey, C., Radu, R., Schepers, D., Simmons, A., Soci, C., Abdalla, S., Abellan, X., Balsamo, G., Bechtold, P., Biavati, G., Bidlot, J., Bonavita, M., Chiara, G., Dahlgren, P., Dee, D., Diamantakis, M., Dragani, R., Flemming, J., Forbes, R., Fuentes, M., Geer, A.,
195   Haimberger, L., Healy, S., Hogan, R. J., Hólm, E., Janisková, M., Keeley, S., Laloyaux, P., Lopez, P., Lupu, C., Radnoti, G., Rosnay, P., Rozum, I., Vamborg, F., Villaume, S., and Thépaut, J.: The ERA5 global reanalysis, Q.J.R. Meteorol. Soc., 146, 1999–2049, https://doi.org/10.1002/qj.3803, 2020.

Pisso, I., Sollum, E., Grythe, H., Kristiansen, N. I., Cassiani, M., Eckhardt, S., Arnold, D., Morton, D., Thompson, R. L., Groot Zwaaftink, C. D., Evangeliou, N., Sodemann, H., Haimberger, L., Henne, S., Brunner, D., Burkhart, J. F., Fouilloux,
200   A., Brioude, J., Philipp, A., Seibert, P., and Stohl, A.: The Lagrangian particle dispersion model FLEXPART version 10.4, Geosci. Model Dev., 12, 4955–4997, https://doi.org/10.5194/gmd-12-4955-2019, 2019.

Seibert, P. and Frank, A.: Source-receptor matrix calculation with a Lagrangian particle dispersion model in backward mode, Atmos. Chem. Phys., 4, 51–63, https://doi.org/10.5194/acp-4-51-2004, 2004.

Verreyken, B., Amelynck, C., Schoon, N., Müller, J.-F., Brioude, J., Kumps, N., Hermans, C., Metzger, J.-M., Colomb, A.,
205   and Stavrakou, T.: Measurement report: Source apportionment of volatile organic compounds at the remote high-altitude Maïdo observatory, Atmos. Chem. Phys., 21, 12965–12988, https://doi.org/10.5194/acp-21-12965-2021, 2021.